A two-surface plasticity model for stiff clay

Pengyun Hong, Jean-Michel Pereira, Anh Minh A.M. Tang, Yu-Jun Cui

Acta Geotechnica manuscript No.
(will be inserted by the editor)

A two-surface plasticity model for stiff clay

P.Y. Hong · J.M. Pereira · A.M. Tang · Y.J. Cui

Received: date / Accepted: date

Abstract This paper presents a constitutive model for describing some important features of the behavior of natural stiff clay evidenced experimentally such as the limited elastic zone, the presence of strain-hardening and softening, and the smooth transition from elastic behavior to a plastic one. The model, namely ACC-2, is an adapted Modified Cam Clay model with two yield surfaces: similarly to Bounding Surface Plasticity theory, an additional yield surface –namely Inner yield surface– was adopted to account for the plastic behavior inside the conventional yield surface. A progressive plastic hardening mechanism was introduced with a combined volumetric-deviatoric hardening law associated with the Inner yield surface, enabling the plastic modulus to vary smoothly during loading paths. The main feature of the proposed model is that its constitutive equations can be simply formulated based on the consistency condition for the Inner yield surface, so that it can be efficiently implemented in a finite element code using a stress integration scheme similar to that of the Modified Cam Clay model. Furthermore, it is proved to be an appropriate model for natural stiff clay: the simulations of a set of tests along different mechanical loading paths on natural Boom Clay show good agreement with the experimental results.

Keywords natural stiff clay; two-surface model; elasto-plasticity; stress integration; validation

1 INTRODUCTION

In comparison with over-consolidated reconstituted clays, natural stiff clays (e.g. Boom Clay, London Clay) exhibit more complex behavior such as a narrow elas-

The first author gratefully acknowledges Chinese Scholarship Council for grant scholarship number: 2009609031

P.Y. Hong · J.M. Pereira (✉) · A.M. Tang · Y.J. Cui
Université Paris-Est, Laboratoire Navier (UMR 8205), CNRS, ENPC, IFSTTAR, F-77455 Marne-la-Vallée, France.
E-mail: jeanmichel.pereira@enpc.fr

tic zone, a smooth transition from elastic behaviour to a plastic one (progressive stiffness degradation with strain) and a complex strain hardening/softening behavior [12, 22, 29]. These features must be taken into account when developing constitutive models for this kind of clays.

Most elasto-plastic constitutive models for soils including the Modified Cam Clay model (MCC) [26] are based on the concept of Critical State [28]. MCC is now widely used for its good description of the main features of soft clay behavior but is not capable of well describing the observed behavior of natural stiff clays [15, 35]. This may be because the conventional yield surface defined in the MCC cannot well capture the yield behavior of natural stiff clay along different loading paths. Note that in this study the terms 'yield surface' and 'yield stress' usually defined in critical state models are referred to as 'conventional yield surface' and 'conventional yield stress' respectively in order to avoid any confusion. Within such a conventional elasto-plastic framework, a number of approaches have been proposed to determine a representative yield stress. Conventional yield points are usually determined based on the sharp slope change in stress vs strain plots such as mean effective stress (p') vs volumetric strain (ε_v), deviator stress (q) vs shear strain (ε_s), or stress work ($\int p' d\varepsilon_v + \int q d\varepsilon_s$) vs stress, etc. [6, 24, 33, 34]. As pointed out by Wood [38], the conventional yield stress can be commonly defined as the intersection point of two linear extrapolations representing the pre-yield and post-yield portions of stress–strain curves.

In the present work, the conventional yield stress is identified from both $p' - \varepsilon_v$ and $q - \varepsilon_s$ curves along each stress path. Taking a standard drained triaxial shear test starting from an isotropic effective stress of 4 MPa on natural Boom Clay at Mol [3] for example, Figure 1 presents the conventional yield point determination. It can be noted that for this test identical conventional yield stresses with $p' = 4.83$ MPa and $q = 2.50$ MPa are determined from both $\log p' - \varepsilon_v$ and $q - \varepsilon_s$ planes. When there is a slight difference between the values determined from the two planes, mean values are determined and considered as the conventional yield stress. The conventional yield points obtained from the triaxial tests and isotropic tests reported in the literature [3, 5, 11, 21] are plotted in Figure 2. The conventional yield curve predicted by the MCC and the corresponding critical state line are also drawn with the parameters (the critical state stress ratio M being 0.67 and initial preconsolidation pressure p'_{c0} being 6 MPa) determined by a classical method proposed by Wood [19]. Inspection of Figure 2 shows that significant difference exists between the MCC surface and the experimental data, showing that the MCC surface is not appropriate for describing the conventional yield behavior of natural Boom Clay along non-isotropic stress paths.

In addition, unrealistic volumetric strains are predicted when an associated flow rule is adopted in MCC: an unrealistic stress-dilatancy relation is obtained for natural stiff clays as will be shown in Section 5. Thereby, to better describe the volumetric strain for natural stiff clays, it is necessary to apply a non-associated flow rule deriving from a plastic potential allowing a wide variety of stress-dilatancy relations. Although efforts have been made to develop such a potential (the plastic potential of MCC being a special case) by e.g. Lagioia *et al.* [20] or McDowell *et al.* [23], progress is still required especially for natural stiff clays.

Besides these issues related to the shape of the yield surface and the non-standard behaviour of natural stiff clays, it must be added that conventional critical state mod-

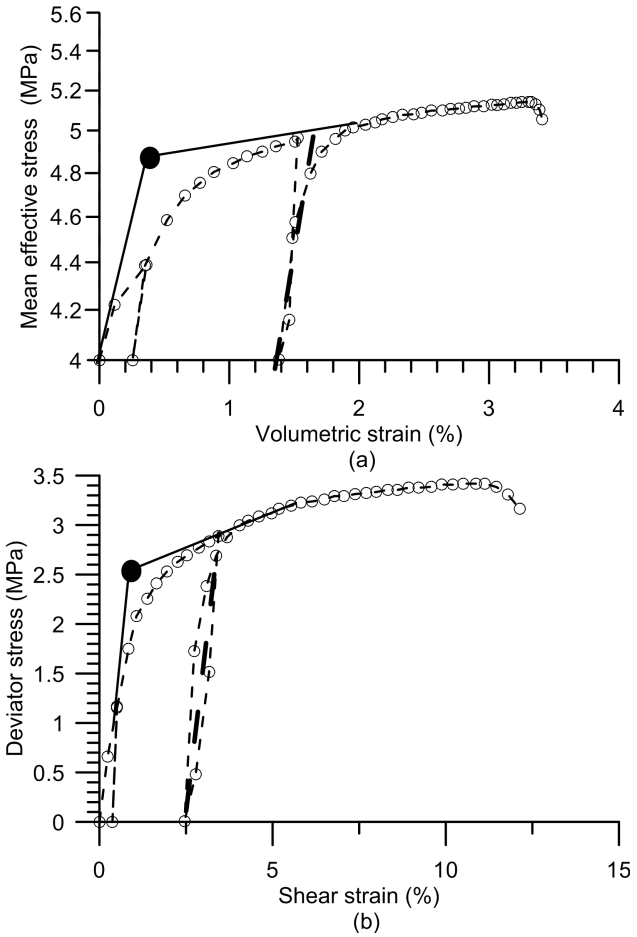

Fig. 1 Conventional yield stress determination from a drained triaxial shear test ($p'_0 = 4.0$ MPa).

els such as MCC are based on a simple elasto-plastic framework, so that they predict a sharp elastic-plastic transition, which departs from smooth elastic-plastic transitions observed experimentally. In order to overcome this difficulty, Dafalias *et al.* [7, 8, 9, 10] introduced the well-known bounding surface model. It is now widely used for describing the smooth transition from elastic to plastic regimes as well as the softening behavior. Within this framework, plastic strains do appear inside the conventional yield surface. It should be noted that the plastic modulus is not obtained by imposing the consistency condition to the associated surface, but is interpolated as a function of the distance between the current stress point and the bounding surface. Lying within the framework of the bounding surface plasticity theory, the concept of sub-loading surface was proposed by Hashiguchi *et al.* [13, 14] and recently extended by Asaoka *et al.* [1, 2] based on Cam Clay model. Similar concepts were extended to account for unsaturated states by Pereira *et al.* [25]. In these models, an additional

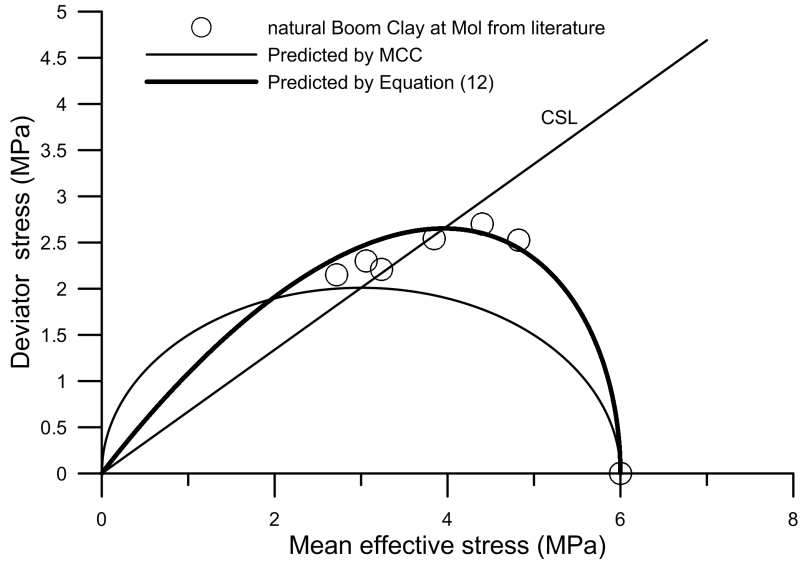

Fig. 2 Conventional yield surface of natural Boom clay: experimental determination and proposed model.

evolution law is introduced to describe soil's structure degradation process from over-consolidated states to normally consolidated states. The plastic strain is taken as an internal variable allowing to describe the softening behavior. Yao *et al.* [39] proposed a unified hardening model (UH model) which can describe the softening behavior of clays by adopting a unified hardening parameter H defined by $dH = \frac{{M_f}^4-\eta^4}{M^4-\eta^4} d\varepsilon_v^p$, with M_f being the potential failure stress ratio and η being the stress ratio q/p'. It is worth noting that such a hardening law implies that the stress state $\eta = M$ is a discontinuity point during the hardening process. This might induce numerical difficulties and thus requires a particular treatment, which is difficult to interpret from a physical point of view.

In this study, an adapted Cam Clay model with two-surface-plasticity (ACC-2) is developed. An extra yield surface (called Inner yield surface) aiming at predicting plastic strain even at small strain levels is introduced to well describe soil behavior inside the existing MCC surface (called Yield surface). Basically, ACC-2 has a structure similar to that of bounding surface models. ACC-2 considers the Inner yield surface as a true yield surface in the sense of conventional elasto-plasticity, incorporating a progressive plastic hardening mechanism. Instead of defining an interpolation function based on the distance to the –outer– Yield surface for the plastic hardening modulus, a specific hardening law associated with the Inner yield surface is defined, enabling the Inner surface to approach without touching the Yield surface and also the plastic modulus to vary smoothly along a plastic loading path. Thereby, the constitutive equations can be simply derived using the consistency condition applied to the Inner yield surface. Hence, in the numerical implementation, all the features of

stress integration schemes for conventional elasto-plastic models can be applied to ACC-2 with only minor modifications.

In this paper, the Two-surface model ACC-2 was firstly presented. Emphasis is put on the development of a new yield surface and a new plastic potential as well as a combined volumetric-deviatoric hardening law for softening behavior description. Then, the constitutive equations were given and the procedure for parameters determination was described. Finally, the model was validated by simulating a set of tests on natural Boom Clay along different loading paths.

2 Model description

For the sake of simplicity, it is assumed that the soil behavior is isotropic. This hypothesis will clearly limit the proposed constitutive model in the case of soils with a strong anisotropy including intrinsic and/or evolving anisotropy. However, the extension of this model to an anisotropic elasto-plastic model is straightforward by incorporating new plastic mechanisms such as an inclined yield surface and a rotational component of hardening law as developed by Wheeler *et al.* [36, 37].

2.1 Elastic behavior

The constitutive model is developed and formulated in the triaxial stress space ($p'-q$). The mean effective stress $p' = p - u$ and the deviator stress q are defined using the effective stress tensor $\sigma'_{ij} = \sigma_{ij} - u\,\delta_{ij}$, $i, j = \{1, 2, 3\}$ as follows (using Einstein's notation repeated indices mean summation):

$$p' = \frac{1}{3}\sigma'_{ij}\delta_{ij} \quad ; \quad q = \sqrt{\frac{3}{2}}\sqrt{s_{ij}s_{ij}} \tag{1}$$

with u, the pore water pressure; δ_{ij}, Kronecker's symbol; and $s_{ij} = \sigma'_{ij} - p'\delta_{ij}$, the deviator stress tensor. By considering compressive stresses as positive, the mean effective stress p' and deviator stress q in the triaxial stress space can be simplify defined as follows:

$$p' = \frac{1}{3}(\sigma'_1 + 2\sigma'_3) \quad ; \quad q = \sigma_1 - \sigma_3 \tag{2}$$

where σ'_1 and σ'_3 are the axial and lateral effective stresses, respectively.

As in MCC model, the elastic volumetric strain increment is given by:

$$d\varepsilon^e_v = \frac{\kappa}{v_0}\frac{dp'}{p'} \tag{3}$$

giving the elastic bulk modulus:

$$K = \frac{v_0}{\kappa}p' \tag{4}$$

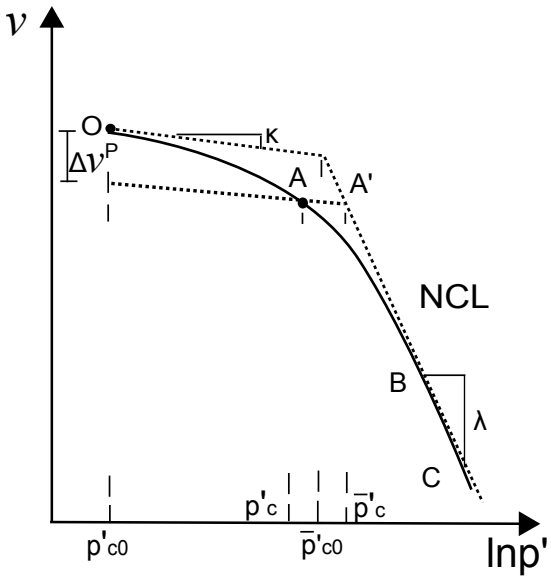

Fig. 3 Schematic representation of the isotropic compression behavior of natural stiff clay.

where κ is the elastic slope in $(\ln p',\, v)$ space and v is the specific volume (v_0 being its initial value at the reference state). The shear strain increment writes as follows:

$$d\varepsilon_s^e = \frac{dq}{3G} \tag{5}$$

With an assumed constant Poisson's ratio ν, shear modulus G can be deduced as:

$$G = \frac{3\,(1-2\nu)}{2\,(1+\nu)}K \tag{6}$$

Even though this choice for the shear modulus (Equation 6) helps in simulating experimental results, it is worth noting that it is not thermodynamically consistent since the Maxwell symmetry relations are not satisfied in this case [18, 41].

2.2 Plastic behavior

2.2.1 Two yield surfaces for a progressive yielding

The isotropic hardening law of MCC is based on the assumption of a bilinear compression curve in $(\ln p' - v)$ plane whereas experimental observations (see Figure 3) have shown that such bilinear relationship is not suitable for describing the smooth transition from the elastic regime to the plastic one as in the case of natural stiff clays (e.g. natural Boom Clay [3]). In this section, an isotropic hardening law that incorporates the plastic mechanism for progressive stiffness degradation is introduced.

The isotropic compression curve of natural stiff clays can be divided into three stages after Smith *et al.* [31]. The first stage corresponds to the 'true' elastic region where the strains are fully recoverable. In general, the size of this region is very small. It has not been represented in Figure 3. In the second stage (O-B), 'true' yield begins to occur since plastic strain is produced. The tangent stiffness is reduced gradually with increasing strain, leading to a smooth compression curve. This behavior is usually termed as 'smooth elasto-plastic transition behavior' (e.g. [7]). In the third stage, large-scale changes in soil particles arrangement occur. The compression behavior in this stage is commonly represented by a normal consolidation line (NCL) with a slope λ as in MCC model.

Any given yield stress state on the compression curve (point A in Figure 3) can be linked to a reference yield state on the NCL (point A$'$ in Figure 3) by a positive scalar r, which is defined as the ratio of the current yield stress to the reference yield stress along an elastic line with slope κ :

$$r = \frac{{p'}_c}{{\overline{p}'}_c} \tag{7}$$

where ${p'}_c$ is the actual loading yield stress and ${\overline{p}'}_c$ is the conventional yield stress on the normal consolidation line.

From this definition, comes straightforwardly the definition of ${\overline{p}'}_c$ and r (or equivalently, ${\overline{p}'}_c$ and ${p'}_c$) as hardening variables that give the size of two distinct yield surfaces (see Figure 4): the conventional yield surface –namely Yield surface– representing the normal consolidation behavior and the Inner yield surface describing the yielding behavior inside the Yield surface. The Yield surface has to be identified as described previously (see Figures 1 and 2). It should be pointed out that the Inner yield surface is defined as a yield limit as in the conventional elasto-plasticity. It has a clear physical meaning since the plastic deformation begins when the stress state reaches it and its evolution verifies the standard Kuhn-Tucker condition. In this regard, the proposed model is similar to the so-called bubble models –but without kinematic hardening–, these models lying also in a framework taking its inspiration from the bounding surface plasticity. Interested readers are referred to the work of Rouainia and Wood [27], among others.

The yield stress on the Inner yield surface in the triaxial stress state is denoted by (p', q) while $(\overline{p}', \overline{q})$ is the corresponding conventional yield stress on the Yield surface (see Figure 4). Since the Inner yield surface is homologous to the Yield surface with respect to the origin in $(p' - q)$ space, therefore:

$$\frac{p'}{\overline{p}'} = \frac{q}{\overline{q}} = \frac{{p'}_c}{{\overline{p}'}_c} = r \tag{8}$$

To achieve a wide variety of yield surface shapes, a generalized yield surface proposed by McDowell [23] is used for the Yield surface (f_Y):

$$f_Y \equiv q^2 + \frac{{M_f}^2}{1 - k_f}\left(\frac{p'}{{\overline{p}'}_c}\right)^{2/k_f} {\overline{p}'}_c^2 - \frac{{M_f}^2 {p'}^2}{1 - k_f} = 0 \ \ (\text{if } \mathrm{k_f} \neq 1) \tag{9}$$

and

$$f_Y \equiv q - M_f p' \sqrt{2\ln({p'}_c/p')} = 0 \ \ (\text{if } \mathrm{k_f} = 1) \tag{10}$$

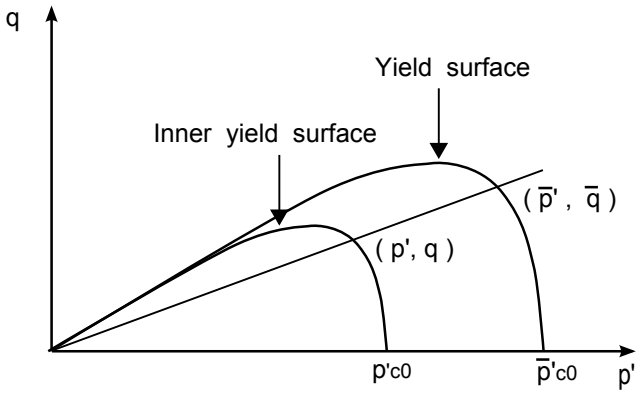

Fig. 4 Yield surfaces of ACC-2 model.

where M_f defines the stress ratio at the apex of the yield surface, k_f is a parameter used to specify the shape of the yield surface. For the sake of brevity but without losing generality, it is assumed that k_f does not equal 1 in the following.

Substituting Equation (9) into Equation (8) gives the mathematical equation of the Inner yield surface (f_I):

$$f_I \equiv r^2 f_Y \tag{11}$$

and therefore:

$$f_I \equiv q^2 + \frac{{M_f}^2}{1-k_f}\left(\frac{p'}{r\overline{p}'_c}\right)^{2/k_f}(r\overline{p}'_c)^2 - \frac{{M_f}^2 p'^2}{1-k_f} = 0 \tag{12}$$

The Inner yield surface has a similar shape and a size r times that of the Yield surface, with $0 \leq r \leq 1$.

2.2.2 Plastic potentials

The expression of the plastic potentials takes the same form as the yield surfaces. The plastic potentials associated with the Inner yield surface and the Yield surface respectively read:

$$g_I(p', q, \beta) \equiv q^2 + \frac{{M_g}^2}{1-k_g}\left(\frac{p'}{r\beta}\right)^{2/kg}(r\beta)^2 - \frac{{M_g}^2 p'^2}{1-k_g} = 0 \tag{13}$$

$$g_Y(p', q, \beta) \equiv q^2 + \frac{{M_g}^2}{1-k_g}\left(\frac{p'}{\beta}\right)^{2/kg}\beta^2 - \frac{{M_g}^2 p'^2}{1-k_g} = 0 \tag{14}$$

giving the flow rule in the case of triaxial compression:

$$\frac{d\varepsilon_v^p}{d\varepsilon_s^p} = \frac{{M_g}^2 - \eta^2}{k_g \eta} \tag{15}$$

where η is the stress ratio q/p', M_g is the critical state slope defining the stress ratio at failure when there is no further volumetric strain increment, k_g is a constant parameter used to control the flow rule (the ratio between plastic volumetric strain increment and plastic shear strain increment), β is the size parameter. This latter can be determined using Equation (13) at any given stress state (p', q) as done by Yu [40]. $k_g = 2$ is the case of MCC with an associated flow rule. For brevity, it is also assumed that k_g is not equal to 1.

In the general case, a non-associated flow rule is considered. If $k_f = k_g$ and $M_f = M_g$, an associated flow rule is recovered. In the former case (i.e. $M_f \neq M_g$), the intersection point between the critical state line and the yield surface is not the apex of the yield surface (as opposed to MCC).

2.2.3 Hardening laws

The two hardening variables $\overline{p}'_c$ and r control the size of the Yield surface and the Inner yield surface, respectively. The evolution of $\overline{p}'_c$ depends on the plastic volumetric strain, as in MCC model, and is described by:

$$d\overline{p}'_c = \frac{v_0}{\lambda - \kappa}\overline{p}'_c d\varepsilon_v^p \tag{16}$$

This equation assumes that the evolution of the Yield surface is induced by volumetric hardening only. Reversely, contribution of the plastic shear strain to plastic hardening is accounted for in the evolution of the Inner yield surface through the evolution law of r, given in incremental form as follows:

$$dr = \frac{v_0}{\lambda - \kappa} s(1 - r) d\varepsilon_d^p \tag{17}$$

where s is a material constant. Since $0 \leq r \leq 1$, Equation (17) shows that r increases monotonically with plastic strain unless its initial value r_0 equals unity, in which case $r = r_0 = 1$ at all times. $(1 - r)$ measures the relative distance between the current yield stress and the reference yield stress. This measure appears in the definition of the plastic modulus, as it is the case for the bounding surface plasticity developed by Dafalias *et al.* [7, 8, 9, 10].

In Equation (17), a generalized plastic strain is used. It is defined as follows:

$$d\varepsilon_d^p = d\varepsilon_v^p + A_d d\varepsilon_s^p \tag{18}$$

where A_d is a parameter which controls the contribution of shear plastic strain. The combined volumetric-deviatoric hardening law given in Equation (17) enables the point representing the stress state to cross the critical state line.

Two distinct situations are encountered depending on the value of r_0:

1. $0 \leq r_0 < 1$: The Inner yield surface is completely inside the Yield surface. When the stress state reaches the Inner yield surface, plastic strain begins and the Inner yield surface and the Yield surface evolve simultaneously according to Equation (16) and Equation (17), respectively. The Inner yield surface moves towards the outer yield surface but without touching it according to the hardening law. The approaching rate depends on the parameter s.

2. $r_0 = 1$: The Inner yield surface and the Yield surface coincide. Both the surfaces evolve at the same rate since $dr = 0$ when $r = r_0 = 1$ according to Equation (17). It is as if the Inner surface was cancelled.

When unloading from the Inner yield surface occurs, purely elastic behavior is assumed as in the conventional elasto-plasticity theory and the stress state moves back inside the Inner yield surface according to the standard Kuhn-Tucker condition. Upon reloading, purely elastic behavior still occurs before the stress state reaches the Inner yield surface again. Obviously, closed hysteresis loops observed experimentally during an unloading-reloading process cannot be predicted in such a framework; however, this is out of the scope of the present study.

2.2.4 Plastic modulus

The prediction of the soil behavior along a certain loading path is reflected by the evolution of the plastic modulus:

$$h = \frac{2{M_f}^2}{k_f} p^{(2/k_f)} (r\bar{p}_c')^{(2-2/k_f)} \frac{v_0}{\lambda - \kappa} \left[\frac{\partial g}{\partial p'} + s(1/r - 1) \left(\frac{\partial g}{\partial p'} + A_d \frac{\partial g}{\partial q} \right) \right] \tag{19}$$

If $r_0 = 1$, MCC model and its corresponding plastic modulus are recovered. Figure 6 illustrates the evolution of the plastic modulus h in the case $0 \leq r_0 < 1$ during a drained conventional triaxial compression test (assuming strain control). The initial effective stress state is represented by point I, which could correspond for instance to the in-situ mean effective stress. When the stress increases below point J (i.e. $\eta < M_g$), $h > 0$ holds as seen in Equation 19 indicating that hardening happens. In this stage, the positive (compressive) plastic volumetric strain and shear strain increments lead to the expansion of both the Yield surface and the Inner yield surface.

When the stress state reaches point J ($\eta = M_g$), the presence of shear hardening part ($\frac{\partial g}{\partial q} > 0$) leads to $h > 0$ even when the effective stress reaches the critical state line with $\frac{\partial g}{\partial p'} = 0$, and hardening thus continues with the effective stress increase across the critical state line. At this state, the Yield surface does not change and the Inner yield surface tends to expand due to the positive shear plastic strain increment.

After point J and before reaching point K, plastic modulus h decreases while remaining positive with the increases of r and η. In this stage, the plastic volumetric strain increment switches from compression to dilation leading to the shrinkage of the Yield surface. The Inner yield surface continues to expand due to the contribution of the shear plastic strain.

When point K is reached, the plastic modulus h becomes null. This point is the transition point from hardening to softening. At this stage, the stress ratio reaches a maximum value and the Inner yield surface has the biggest size.

After point K (peak of deviator stress), the plastic modulus becomes negative with the increase of r. The stress state moves downwards as soil's shear resistance decreases. Both the Yield surface and the Inner yield surface shrink. The critical

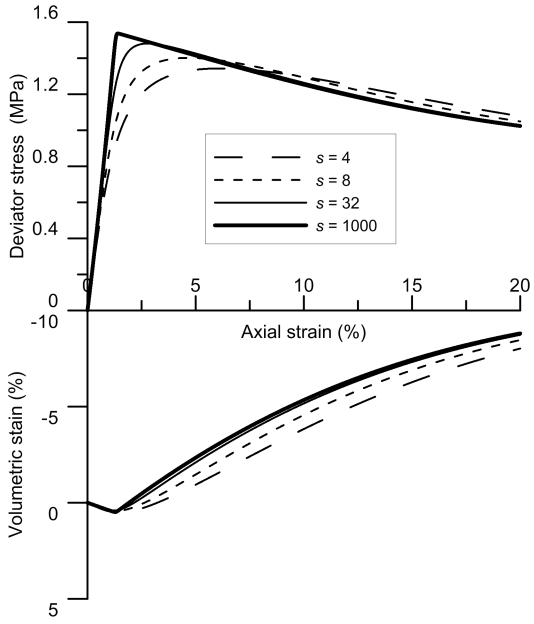

Fig. 5 Variation of stress–strain curves with material constant s.

state (point L) is reached asymptotically with r tending to 1 and the increments of hardening variables (dr and $d\overline{p}'_c$) tending to 0.

Accounting for the contribution of r, the evolution of plastic modulus and thus the shape of stress-strain curve can be controlled by the material constant s as shown in Figure 5 , which presents the stress–strain curves predicted by the model for a standard drained triaxial compression test from an initial isotropic stress state with $p' = 1$ MPa. In the simulations, s varies between 4 and 1000. $A_d = 1$ is considered and the other model parameters can be found in Table 1. The figure also shows that if large values are used for s (e.g. $s = 1000$), the model gives results similar to conventional elastic-plastic model.

2.3 Incremental stress-strain relation

Plastic strain is generated if the Inner yield surface is activated. The plastic strain increment is computed from the plastic potential using the flow rule:

$$d\boldsymbol{\varepsilon}^p = d\lambda \frac{\partial g_I}{\partial \boldsymbol{\sigma}'} \tag{20}$$

where $d\lambda$ is the plastic multiplier, and g_I is the plastic potential corresponding to the (activated) Inner yield surface.

Gathering hardening variables $\overline{p}'_c$ and r in a single vector denoted $\boldsymbol{X}$ and defined by:

$$\boldsymbol{X} = \{X_1, X_2\}^t = \{\overline{p}'_c, r\}^t \tag{21}$$

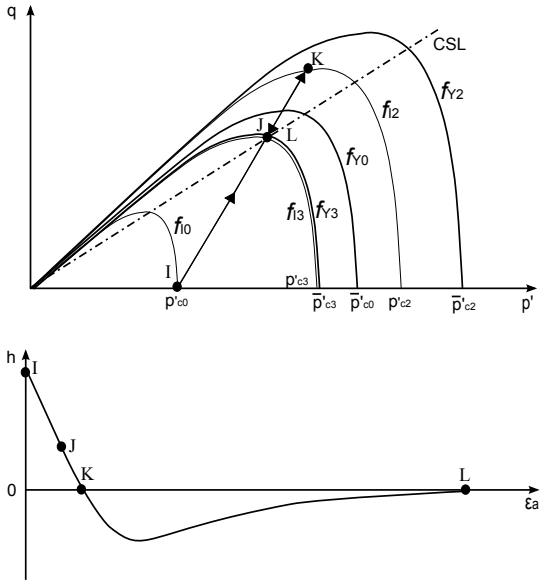

Fig. 6 Evolution of plastic modulus along a drained conventional triaxial loading path.

the hardening law can be written in the following general form:

$$d\boldsymbol{X} = d\lambda \boldsymbol{B} \tag{22}$$

where:

$$\boldsymbol{B} = \{B_1, B_2\}^t \tag{23}$$

$$B_1 = \frac{\partial \overline{p}'_c}{\partial \varepsilon_v^p} \frac{\partial g_I}{\partial p'} \tag{24}$$

$$B_2 = \frac{\partial r}{\partial \varepsilon_d^p} \left(\frac{\partial g_I}{\partial p'} + A_d \frac{\partial g_I}{\partial q} \right) \tag{25}$$

The consistency condition applied to the Inner surface leads to:

$$\left(\frac{\partial f_I}{\partial \boldsymbol{\sigma}'} \right)^t : d\boldsymbol{\sigma}' - h d\lambda = 0 \tag{26}$$

with h being the hardening modulus:

$$h = -\left(\frac{\partial f_I}{\partial \overline{p}'_c} B_1 + \frac{\partial f_I}{\partial r} B_2 \right) \tag{27}$$

The differential stress-strain equations can finally be obtained:

$$\begin{aligned} d\boldsymbol{\sigma}' &= \boldsymbol{D}_{ep} d\boldsymbol{\varepsilon} \\ d\boldsymbol{X} &= \boldsymbol{R}_{ep} d\boldsymbol{\varepsilon} \end{aligned} \tag{28}$$

where:

$$\boldsymbol{D}_{ep} = \boldsymbol{D}_e - \frac{\boldsymbol{D}_e \boldsymbol{b} (\boldsymbol{a})^t \boldsymbol{D}_e}{(\boldsymbol{a})^t \boldsymbol{D}_e \boldsymbol{b} + h} \tag{29}$$

$$\boldsymbol{R}_{ep} = (\boldsymbol{R}_{ep1}, \boldsymbol{R}_{ep2})^t \tag{30}$$

$$\boldsymbol{R}_{ep1} = \frac{B_1 (\boldsymbol{a})^t \boldsymbol{D}_e}{(\boldsymbol{a})^t \boldsymbol{D}_e \boldsymbol{b} + h} \tag{31}$$

$$\boldsymbol{R}_{ep2} = \frac{B_2 (\boldsymbol{a})^t \boldsymbol{D}_e}{(\boldsymbol{a})^t \boldsymbol{D}_e \boldsymbol{b} + h} \tag{32}$$

and $\boldsymbol{D}_e$ is the elastic stiffness matrix, $\boldsymbol{a} = \dfrac{\partial f_I}{\partial \boldsymbol{\sigma'}}$, $\boldsymbol{b} = \dfrac{\partial g_I}{\partial \boldsymbol{\sigma'}}$.

3 Stress integration algorithm

The explicit stress integration scheme with an adaptive time-stepping scheme (see Sloan *et al.* [30]) is used here to solve the above stress-strain relations. It is worth noting that consideration of the Inner yield surface (f_I) is sufficient even though two yield surfaces co-exist. Thus, the implementation of ACC-2 is similar to that of MCC. This is because:

1. The Inner yield surface is treated as a 'true' yield surface in the sense of conventional plasticity. All the features of the stress integration schemes (e.g. loading criterion) for the classic elasto-plastic models can be applied to the Inner yield surface.
2. In the general case $0 \leq r_0 < 1$, the definition of the hardening laws ensures that the effective stress never reaches the Yield surface.
3. If $r_0 = 1$, the Inner yield surface and the Yield surface coincide at any stress state and the same constitutive relations are determined from the consistency condition for any of the two yield surfaces. Thereby, only one yield surface requires to be solved.

For a plastic loading process, the increments of stress and hardening parameters can be calculated using an Euler solution and a modified Euler solution. The error is calculated by taking the difference between the two solutions. The size of the increment can be adapted automatically by maintaining the local integration error below a specified tolerance. Since two hardening variables are associated with the Inner yield surface, the error measure R with respect to the hardening variables is evaluated as follows:

$$R = \sqrt{\frac{\left(\overline{p}'_{c1} - \overline{p}'_{c2}\right)^2}{\left(\overline{p}'_{c2}\right)^2} + \frac{\left(r_1 - r_2\right)^2}{\left(r_2\right)^2}} \tag{33}$$

where subscripts 1 and 2 denote values obtained by Euler solution and modified Euler solution, respectively. A detailed presentation of the integration algorithm can be found in the original work by Sloan *et al.* or in extensions of it (e.g. [16]).

4 Determination of parameters

The proposed model ACC-2 have 11 parameters (λ, κ, ν, $\overline{p}'_{c0}$, k_f, M_f, k_g, M_g, s, r_0, A_d). The procedure for determining these parameters is described below.

1. λ, κ, $\overline{p}'_{c0}$, ν, M_g are common parameters of MCC and can be determined in a common fashion. λ is the slope of normal consolidation compression line and κ is the slope of swelling line of the isotropic compression curve in $\ln p' - v$ plane. Note that $\overline{p}'_{c0}$ in ACC-2 denotes conventional isotropic preconsolidation pressure which defines the initial size of the Yield surface. These three parameters (λ, κ and $\overline{p}'_{c0}$) can be determined by an isotropic compression test as indicated in Figure 3. Poisson's ratio ν can be determined from a triaxial test by considering the elastic behaviour (at a low strain level around 0.5%) in the $\varepsilon_1 - \varepsilon_v$ plane: $\nu = (1 - \varepsilon_v/\varepsilon_1)/2$. M_g is the critical state stress ratio and it can be determined by the effective stress ratio at the critical state along different loading paths.
2. M_f and k_f are parameters affecting the shape of the yield surface which can be calibrated by fitting the conventional yield surface shape to the conventional yield points in different radial directions in $p' - q$ plane (see Figure 2).
3. k_g is used to describe the plastic flow rule and can be determined by the values of $d\varepsilon_v^p/d\varepsilon_s^p$ obtained from drained triaxial shear tests.
4. r_0 specifies the size of Inner yield surface associated with the first occurrence of plastic strains. For natural stiff clay, the initial size of the Inner yield surface is defined by the initial in-situ mean effective stress. It is worth noting that in that case r_0 corresponds to the inverse of the overconsolidation ratio (OCR), as classically defined.
5. Parameter s determines the hardening rate of Inner yield surface in approaching the Yield surface. It influences the variation rate of the plastic modulus. This parameter can be calibrated from an isotropic compression test.
6. A_d controls how plastic shear strain affects the hardening process. It can be obtained by fitting the experimental results, especially the ones showing softening.

5 Prediction and validation

In this section, the performance of ACC-2 is assessed by predicting the behavior of natural Boom Clay based on experimental data available in the literature. Boom clay (160 to 270 m deep) under the Mol-Dessel nuclear site is considered as a possible host formation in the Belgian program on geological disposal for nuclear waste disposal. The samples are taken at a depth of 223 m from the underground research facility of Mol. At this depth, the total vertical stress is around 4.5 MPa and the pore pressure is equal to 2.2 MPa, defining an effective stress of 2.3 MPa [4]. Based on in-situ stress estimations [17], the initial ratio of the horizontal effective stress to the vertical one is about 0.8. The in situ effective stress state can thus reasonably be approximated by an isotropic stress state, to be used as the initial effective stress state when performing laboratory tests.

A number of experimental results show that the saturation process used during the sample preparation plays an important role in the mechanical response of nat-

Table 1 ACC-2 parameters for natural Boom Clay.

λ	κ	ν	$\overline{p}'_{c0}$ (MPa)	M_f	k_f
0.18	0.02	0.3	6	0.67	0.7
M_g	k_g	r_0	s	A_d	
0.67	0.90	0.33	8	0.1	

Table 2 Summary of the isotropic and oedometric tests reported in the literature.

Test	Reference	Void ratio after saturation	Effective stress path (MPa)
Iso-1	Baldi *et al.* [3]	0.677	$2 \rightarrow 4 \rightarrow 2 \rightarrow 8 \rightarrow 2 \rightarrow 5$
Iso-2	Le [21]	0.590	$2.5 \rightarrow 10 \rightarrow 2.5$
Iso-3	Deng *et al.* [11]	0.610	$2.3 \rightarrow 20 \rightarrow 7$
Oed-1	Baldi *et al.* [3]	0.733	$2 \rightarrow 10$

ural Boom Clay. Significant swelling occurs while saturating specimens under low effective stresses (referred to as Process I) [3, 5, 21, 32]. The microstructure changes induced by this swelling are at the origin of experimental artefacts, such as an underestimated preconsolidation pressure (e.g. 0.37 MPa, that is lower than the in-situ effective stress [32]). Realizing that swelling may alter the mechanical behavior of natural Boom Clay, Baldi *et al.* [3] improved the saturation process and reduced this relatively high swelling by loading the sample to the in-situ effective stress state (around 2.3 MPa) under drained conditions prior to injection of water for saturation (referred to as Process II). Therefore, only the data obtained from experiments following Process II are representative of the behavior of natural Boom Clay, and will be considered in this study. The results that are taken into account include those from isotropic compression tests and drained triaxial shear tests, carried out in different laboratories.

All the simulations are performed starting from a common point (p'_0 = 2 MPa, e_0 = 0.61). For comparison purposes, the predictions by MCC are also presented. The model parameters of ACC-2 for natural Boom Clay are presented in Table 1, including the five common parameters of MCC as described in Section 4. The parameters λ, κ, $\overline{p}'_{c0}$, s were determined using isotropic compression tests (Iso-1, Iso-2 and Iso-3); k_g, A_d, ν were calibrated using the experimental curve ($\varepsilon_v - \varepsilon_1$) of two drained triaxial shear tests (CD-1 and CD-2 as seen afterwards); M_f, k_f and M_g were derived from the conventional yield stresses and the critical stress ratio of the four drained triaxial shear tests (CD-1, CD-2, CD-3 and CD-4), respectively. The oedometer test (Oed-1) and the drained triaxial test (CD-5) were excluded from the parameter determination process.

5.1 Isotropic test

Various isotropic compression tests on natural Boom Clay have been performed, some of which are considered in this work and summarized in Table 2. After comple-

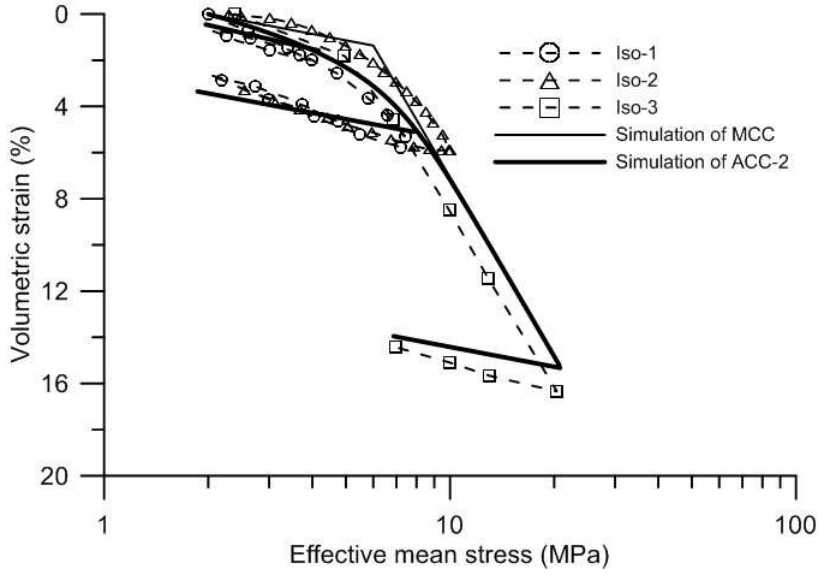

Fig. 7 Numerical simulations of isotropic tests.

tion of the saturation process, one (or more) isotropic compression-decompression cycles were applied to the specimen under drained conditions as described in the aforementioned table. For all of these tests, volumetric strains were obtained from the volume of drained-out water.

Figure 7 compares the simulations of isotropic tests by both MCC and ACC-2. It is worth noting that the experimental data presents some scatter. As a matter of fact, the simulations cannot satisfy all the tests. Keeping this in mind, it can be noticed that ACC-2 captures satisfactorily the general trend shown by the clay during both loading and unloading processes (neglecting the hysteretic behavior). At low stress levels ($p' < 10$ MPa), the curve predicted by ACC-2 is as smooth as the experimental curves, which is not the case for MCC. At high stress levels ($p' > 10$ MPa), both ACC-2 and MCC predict the same response. For the unloading process from $p' = 4$ MPa, it appears that MCC cannot predict the irrecoverable strain observed experimentally, since purely elastic strains are assumed in this range of stress. On the opposite, ACC-2 can predict such irrecoverable strains.

5.2 Oedometer test

Oedometer test (Oed-1) performed by Baldi *et al.* (see Table 2 [3] was simulated. The specimen was saturated under a vertical effective stress of 2 MPa. The vertical effective stress was then increased to 10 MPa.

Figure 8 shows the corresponding predictions by MCC and ACC-2. It can be observed clearly that the curve simulated using ACC-2 agrees well with the experimental curve, and better than the one obtained with MCC. This shows the relevance

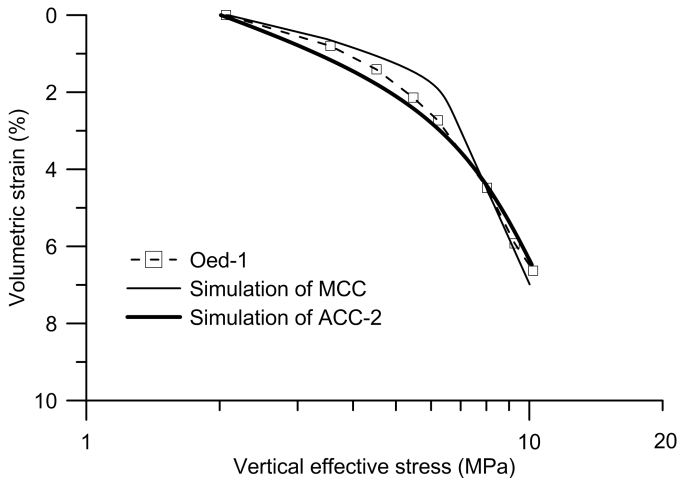

Fig. 8 Numerical simulations of oedometer test.

Table 3 Summary of the drained triaxial tests reported in the literature.

Test	Reference	Initial water content (%)	Mean effective stress after saturation / before shearing (MPa)	Void ratio after saturation	Shear rate (μm/min)	Axial strain before unloading-reloading cycle
CD-1	Baldi *et al.* [3]	25.8	2.0 / 2.0	0.705	1.00	0.6% and 2.8%
CD-2	Le [21]	19.6	2.5 / 2.5	0.590	1.00	–
CD-3	Baldi *et al.* [3]	25.8	2.0 / 3.0	0.717	1.00	0.6% and 2.1%
CD-4	Le [21]	20.0	2.5 / 3.5	0.560	0.90	–
CD-5	Baldi *et al.* [3]	25.7	2.0 / 4.0	0.712	1.00	0.6% and 3.8%

of ACC-2 in simulating a compression test under K_0 condition. The curve predicted by ACC-2 highlights again the capability of ACC-2 in simulating smooth stress-strain behavior as observed experimentally.

In this test, a K_0 value of 0.755 is predicted by ACC-2, whereas $K_0 = 0.856$ is predicted by MCC in the normally consolidated state. This difference is mainly attributed to the fact that a non-associated flow rule is assumed in ACC-2 while an associated flow rule is used in MCC. ACC-2 and MCC predict the same value of K_0 in the case that $k_g = 2$ with an associated flow rule. In addition, the predicted values of these two models are close to the K_0 value of 0.8 determined by Horseman *et al.* [17] based on in situ stress conditions.

5.3 Drained triaxial test

The drained triaxial compression tests (CD) considered in this study are summarized in Table 3 [3, 21]. After saturation following Process II, the effective stress path consists of an isotropic consolidation (except for tests CD-1 and CD-2) followed by

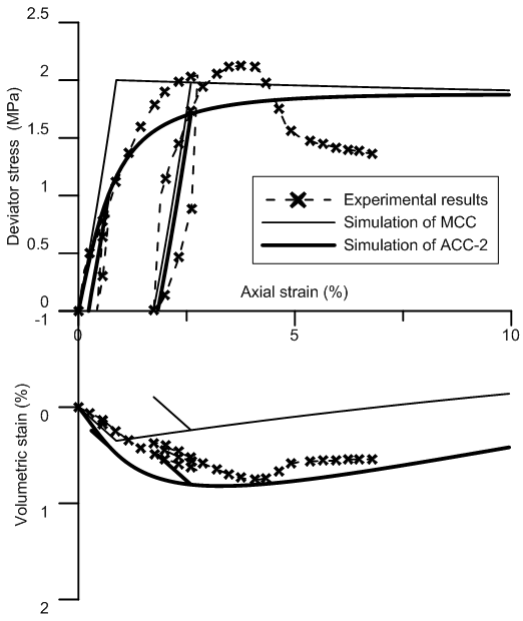

Fig. 9 Numerical simulations of drained triaxial shear test CD-1 (p'_0=2.0 MPa).

a triaxial shear stage. In some of these tests, unloading-reloading cycles were applied during the shearing stage (see Table 3.

These tests have been simulated using ACC-2 and MCC, starting after the saturation stage. Figures 9 to 13 compare the obtained predictions, for the shear stage only. The results are presented in terms of variations of deviator stress and volumetric strain versus axial strain.

For test CD-1, though underpredicting the conventional yield stress as does MCC, ACC-2 gives smoother simulation results and agrees better with the experimental results as shown in Figure 9. Further, both MCC and ACC-2 predict the shear dilatancy behavior on the volumetric strain-axial strain curve but the latter one gives better results for volumetric strain. The reason is that the soil response shows a marked softening behaviour (at about $4.5 - 6.8\%$) that MCC and ACC-2 models cannot predict satisfactorily. In the case of ACC-2, this is because the value of A_d has been determined based on the complete set of tests, in order to predict the whole softening/hardening behavior along different loading paths. Regarding the unloading-reloading cycles, ACC-2 can predict the observed irrecoverable strain for both cycles, either from a small strain ($\varepsilon_1 = 0.6\%$) or from larger strain ($\varepsilon_1 = 2.8\%$). Reversely, MCC only predicts such behavior for the cycle starting from the largest axial strain. Disregarding the hysteretic behavior during these cycles, it can be observed that both models capture well the unloading-reloading slope of the stress-strain curve.

Figure 10 indicates that the predictions of test CD-2 test by ACC-2 are consistently better than those by MCC for both the deviator stress–axial strain and volumetric strain–axial strain relationships. This suggests that ACC-2 can capture well

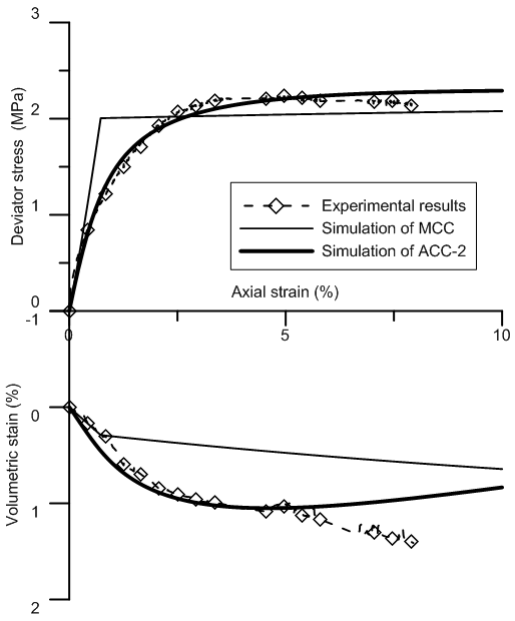

Fig. 10 Numerical simulations of drained triaxial shear test CD-2 (p'_0=2.5 MPa).

the smooth elasto-plastic transition of the deviator stress–axial strain curve. Again, the predictions of volume change are greatly improved by ACC-2 as compared to MCC.

For test CD-3, the predictions by ACC-2 agree well with the experimental results with a smooth elasto-plastic transition observed for the deviator stress–axial strain curve as shown in Figure 11. These results show that the conventional yield point in terms of deviator stress is well captured by ACC-2, in agreement with the choice of the new yield surface. Even though the volumetric strain prediction by ACC-2 does not fully agree with the experimental results, comparison with the prediction by MCC shows that ACC-2 can better predict the volume change of natural Boom clay.

As shown in Figure 12, a small difference appears between the predicted results of ACC-2 and the experimental observations for test CD-4. However, the general trend of the smooth stress strain curve can be captured by ACC-2. Moreover, the volumetric strain prediction is greatly improved by ACC-2 in comparison to MCC.

For test CD-5, it appears that the predictions by ACC-2 agree quite well with the experimental results for the deviator stress–axial strain relationship as shown in Figure 13. For the volumetric strain, ACC-2 gives relatively larger values at small axial strain levels but relatively smaller values at larger axial strain levels.

In summary, compared to MCC, ACC-2 provides better predictions for natural Boom Clay under drained triaxial loading conditions. It has been found that ACC-2 is good at conventional yield shear stresses prediction with the adoption of a new expression for the yield surface. The smooth elasto-plastic transition and realistic shear dilatancy can be well predicted by ACC-2. This shows that the plastic mechanism that

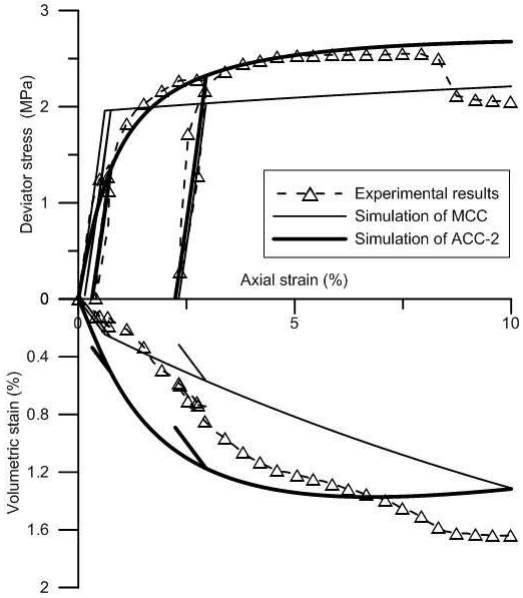

Fig. 11 Numerical simulations of drained triaxial shear test CD-3 (p'_0=3.0 MPa).

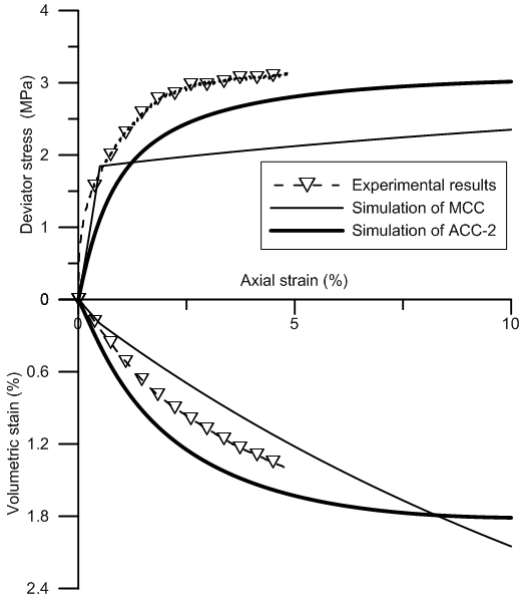

Fig. 12 Numerical simulations of drained triaxial shear test CD-4 (p'_0=3.5 MPa).

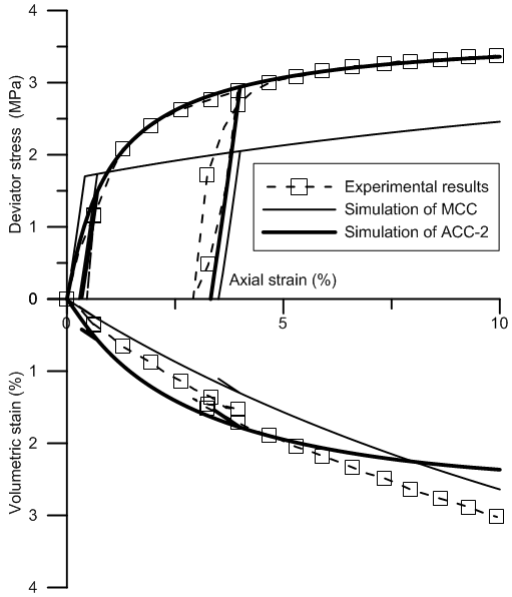

Fig. 13 Numerical simulations of drained triaxial shear test CD-5 (p'_0=4.0 MPa).

allows flexible plastic modulus variation with the stress state inside the conventional yield surface is suitable for describing the natural Boom Clay behavior. In addition, the volumetric strain is better described by ACC-2. It should be pointed out that ACC-2 model can significantly improve the prediction of tests with monotonic loading, but still cannot predict the hysteresis loop observed during unloading/reloading cycles. This is because it predicts only an elastic strain rate in the unloading process. A better prediction of unloading/reloading behavior could be obtained by assuming an additional plastic mechanism in the unloading/reloading process.

5.4 Undrained triaxial test

To investigate the performance of the model in predicting the undrained behavior of soils, a series of triaxial shear tests are simulated. Two conventional undrained triaxial compression tests (CU-1 and CU-2) from different starting stress states and a conventional undrained triaxial extension test (CUE-1) are considered. In CU-1, the sample is first isotropically consolidated up to a mean effective stress of 10 MPa and then sheared from this stress state in undrained condition. In CU-2 and CUE-1, the samples are first consolidated under K_0 condition up to a vertical effective stress of 10 MPa (which corresponds to test Oed-1 presented in Section 5.2),then they are sheared to failure in undrained compression and undrained extension conditions, respectively. In this study, the slope of the critical state line in extension ($q < 0$) and in compression are assumed equal ($q > 0$).

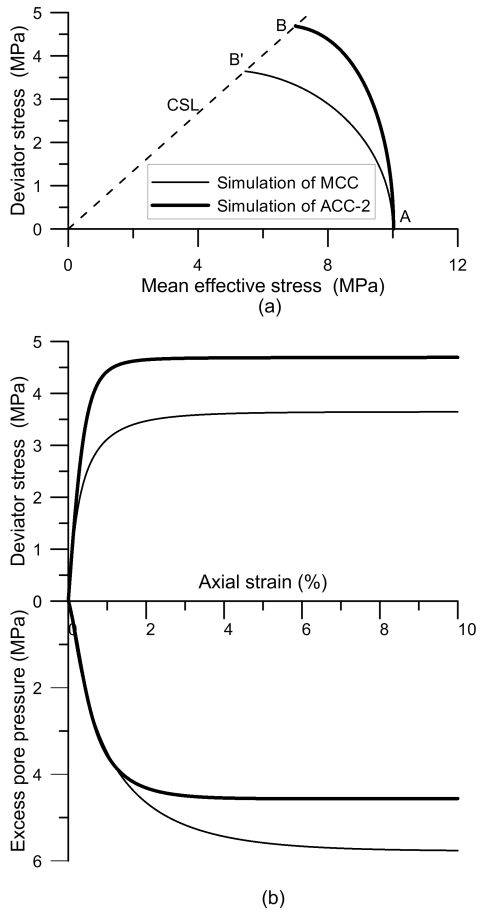

Fig. 14 Numerical simulations of undrained triaxial shear test CU-1.

Figure 14 compares the undrained effective stress paths and the stress-strain curves of CU-1 predicted by ACC-2 and MCC. After the isotropic consolidation process, the samples are in the normally consolidated state (point A in Figure 14(a)) for both ACC-2 and MCC. At this point, variable $r = 1$, and the Yield surface and Inner Yield Surface coincide for ACC-2. As shown in Figure 14(a), the effective stress paths predicted by ACC-2 and MCC follow approximately their respective yield surface until the critical state line (CSL) is reached. Even though the critical state line has the same slope for both models, ACC-2 predicts an undrained shear strength different from MCC, since different yield surfaces are considered. No softening behavior is observed since the clays are in the normally consolidated state. The stress–strain curves ($q - \varepsilon_1$ plot in Figure 14(b)) predicted by ACC-2 and MCC also develop similarly, even though ACC-2 predicts higher deviator stresses. In both cases, the deviator stress first varies quickly with the axial strain before increasing more gradually as the effective stress path comes closer to the CSL, where it reaches a plateau.

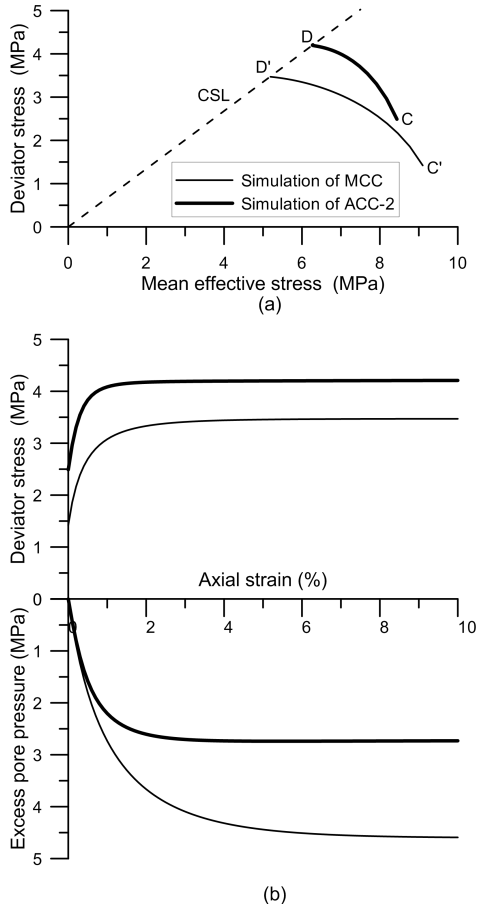

Fig. 15 Numerical simulations of undrained triaxial shear test CU-2.

Simulation of test CU-2 is shown in Figure 15. It can be observed that different stresses at the start of the undrained shear stage are obtained, resulting from different predictions in the preceding K_0 consolidation process as shown in Section 5.2: $p' = 8.4$ MPa, $q = 2.5$ MPa for ACC-2 (point C in Figure 15(a)) and $p' = 9.1$ MPa, $q = 1.4$ MPa for MCC (point C$'$ in Figure 15(a)). Previous comments on test CU-1 mainly apply to the predictions of the shear stage of test CU-2 by the two models.

Figure 16 shows the simulation results for the triaxial extension test CUE-1. As shown in Figure 16(a), the effective stress paths predicted by MCC and ACC-2 are vertical before the corresponding yield surfaces is reached in the extension side. After reaching the yield surface, the effective stress paths follow approximately the yield surfaces until they reach the CSL. In $q - \varepsilon_1$ plot (see Figure 16(b)), the axial strains develop in the extension direction. In the initial stage, the deviator stress varies linearly with the axial strain since purely elastic behavior is predicted by both models.

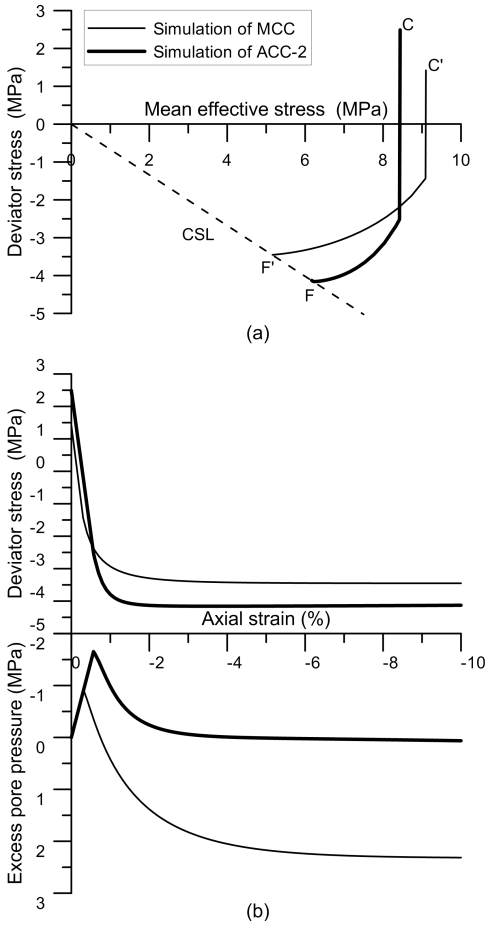

Fig. 16 Numerical simulations of undrained triaxial shear test CUE-1.

5.5 Critical state line

Critical state is defined in ACC-2 as it is in MCC. Critical state is reached with an effective stress ratio $\eta = \pm M_g$. At these states, plastic shearing could continue indefinitely without volume and effective stress changes. To investigate the critical state predicted by ACC-2, drained and undrained tests under triaxial compression and extension on normally consolidated and overconsolidated samples are considered. The tests include the previous triaxial tests (CD-1, CD-2, CD-3, CD-4, CD-5, CU-1, CU-2, and CUE-1) and two additional drained triaxial extension tests (CDE-1 and CDE-2). In CDE-1 and CDE-2, the samples were sheared under triaxial extension conditions after an isotropic loading up to 2 MPa and 4 MPa, respectively.

All the critical states from the simulations are plotted in the effective stress plane $p' - q$ (Figure 17(a)) and the compression plane $(p' - e)$ (Figure 17(b)). It can be seen

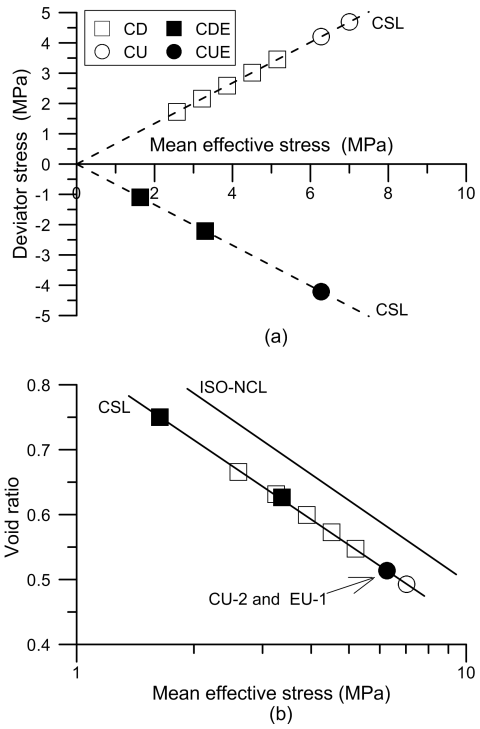

Fig. 17 CSL of triaxial compression and extension in (a): $p' - q$ plane and (b): $\log p' - e$ plane.

that the critical states lie on the lines of $\eta = \pm M_g$ in the $p' - q$ plane and can be described by a unique CSL in the $\log p' - e$ plane, irrespective of the consolidation history, stress path (compression or extension), and drainage condition.

6 Conclusion

A constitutive model with two surfaces –ACC-2– is developed for describing some important features of the behavior of natural stiff clays. The model ACC-2 uses new general expressions of the yield and plastic potential, with Modified CamClay –MCC– yield surface being a special case. To account for the plastic behavior inside the conventional yield surface, a new plastic mechanism is proposed based on an additional yield surface, namely Inner yield surface. A hardening law associated with the Inner yield surface is introduced, enabling the plastic modulus to vary flexibly when the stress approaches the Yield surface. This hardening law ensures that the Inner yield surface approaches but never crosses the conventional Yield surface. Both volumetric and deviatoric plastic strains are accounted for in the hardening law so that the model can describe the softening behavior. The constitutive equation of the model can be simply formulated based on the consistency condition for the Inner yield surface. Since only the Inner yield surface has to be treated, ACC-2 can be

efficiently implemented using a stress integration scheme similar to MCC. Comparisons with experimental results on natural Boom Clay suggest that ACC-2 is able to capture the overall stress-strain behavior along different loading paths and therefore constitutes a useful tool for describing the behavior of natural stiff clays.

References

1. Asaoka A (2005) Compaction of sand and consolidation of clay: a super/subloading yield surface approach. In: Proc. 11th Int. Conference IACMAG, vol 4, pp 121–140
2. Asaoka A, Nakano M, Noda T (2000) Superloading yield surface concept for highly structured soil behavior. Soils and Foundations 40(2):99–110
3. Baldi G, Hueckel T, Peano A, Pellegrini R (1991) Developments in modelling of thermo-hydro-geomechanical behaviour of boom clay and clay-based buffer materials. Commission of the European Communities, Nuclear Science and Technology p EUR 13365/1 and EUR 13365/2
4. Bernier F, Li XL, Bastiaens W (2007) Twenty-five years' geotechnical observation and testing in the tertiary boom clay formation. Géotechnique 57(2):229–237
5. Coll C (2005) Endommagement des roches argileuses et perméabilité induite au voisinage d'ouvrages souterrains. PhD thesis, Université Joseph-Fourier-Grenoble I
6. Cui YJ, Delage P (1996) Yielding and plastic behaviour of an unsaturated compacted silt. Géotechnique 46(2):291–311
7. Dafalias Y (1986) Bounding surface plasticity. i: Mathematical foundation and hypoplasticity. Journal of Engineering Mechanics 112(9):966–987
8. Dafalias Y, Herrmann L (1980) A bounding surface soil plasticity model. In: International Symposium on Soils under Cyclic and Transient Loading, Swansea, UK, vol 1, pp 335–345
9. Dafalias Y, Popov E (1975) A model of nonlinearly hardening materials for complex loading. Acta Mechanica 21(3):173–192
10. Dafalias Y, Popov E (1976) Plastic internal variables formalism of cyclic plasticity. Journal of applied mechanics 43(4):645–651
11. Deng YF, Tang AM, Nguyen X, Cui YJ (2011) Hydro-chemo-mechanical characterization of boom clays at essen. Post-doc report
12. Gasparre A (2005) Advanced laboratory characterisation of london clay. PhD thesis, Imperial College London
13. Hashiguchi K (1978) Plastic constitutive equations of granular materials. In: Proc. US–Japan seminar on continuum mechanical and statistical approaches in the mechanics of granular materials (eds SC Cowin and M. Satake), pp 321–329
14. Hashiguchi K (1989) Subloading surface model in unconventional plasticity. International Journal of Solids and Structures 25(8):917–945
15. Hong PY (2013) Development and explicit integration of a thermo-mechanical model for saturated clays. PhD thesis, École Nationale des Ponts et Chaussées

16. Hong PY, Pereira JM, Cui YJ, Tang AM (2012) Explicit integration of a thermo-mechanical model for clays. Computers and Geotechnics 46(0):13 – 25
17. Horseman S, Winter M, Entwisle D (1993) Triaxial experiments on boom clay. The Engineering Geology of Weak Rock pp 36–43
18. Houlsby G, Puzrin A (2006) Principles of hyperplasticity: an approach to plasticity theory based on thermodynamic principles. Springer
19. Houlsby G, Wroth C, Wood D (1983) Predictions of the results of laboratory tests on a clay using a critical state model. International workshop on constitutive relations for soils pp 99–121
20. Lagioia R, Puzrin A, Potts D (1996) A new versatile expression for yield and plastic potential surfaces. Computers and Geotechnics 19(3):171–191
21. Lê T (2008) Comportement thermo-hydro-mécanique de l'argile de boom. PhD thesis, École Nationale des Ponts et Chaussées
22. Li XL, Bernier F, Vietor T, Lebon P (2011) Thermal impact on the damaged zone around a radioactive waste disposal in clay host rocks-technical annex 1. Final report to EC (Contract Number: FI6W-CT-2007-036449) EUR
23. McDowell G, Hau K (2004) A generalised modified cam clay model for clay and sand incorporating kinematic hardening and bounding surface plasticity. Granular Matter 6(1):11–16
24. Mitchell R (1970) On the yielding and mechanical strength of leda clays. Canadian Geotechnical Journal 7(3):297–312
25. Pereira JM, Rouainia M, Manzanal D (2014) Combined effects of structure and partial saturation in natural soils. Journal of Geo-engineering Sciences 2(1-2):3–16, DOI 10.3233/JGS-141312
26. Roscoe K, Burland J (1968) On the generalised stress-strain behaviour of "wet" clay. In: Heyman J, Leckie FA, editors. Engineering plasticity, Cambridge University Press, pp 535–609
27. Rouainia M, Wood D (2000) A kinematic hardening constitutive model for natural clays with loss of structure. Géotechnique 50(2):153–164
28. Schofield A, Wroth P (1968) Critical state soil mechanics
29. Simpson B (2010) Engineering in stiff sedimentary clays. Géotechnique 60(12):903–911
30. Sloan S, Abbo A, Sheng D (2001) Refined explicit integration of elastoplastic models with automatic error control. Engineering Computations 18(1-2):121–154
31. Smith P, Jardine R, Hight D (1992) The yielding of bothkennar clay. Géotechnique 42(2):257–274
32. Sultan N (1997) Etude du comportement thermo-mécanique de l'argile de boom: expériences et modélisation. PhD thesis, École Nationale des Ponts et Chaussées
33. Tavenas F, Leroueil S, La Rochelle P, Roy M (1978) Creep behaviour of an undisturbed lightly overconsolidated clay. Canadian Geotechnical Journal 15(3):402–423
34. Tavenas F, Des Rosiers J, Leroueil S, La Rochelle P, Roy M (1979) The use of strain energy as a yield and creep criterion for lightly overconsolidated clays. Geotechnique 29(3):285–303

35. Valls-Marquez M (2009) Evaluating the capabilities of some constitutive models in reproducing the experimental behaviour of stiff clay subjected to tunnelling stress paths. PhD thesis, The University of Birmingham
36. Wheeler S (1997) A rotational hardening elasto-plastic model for clays. In: Proceedings of the International Conference on Soil Mechanics and Foundation Engineering, AA BALKEMA, vol 1, pp 431–434
37. Wheeler S, Naatanen A, Karstunen M, Lojander M (2003) An anisotropic elasto-plastic model for soft clays. Canadian Geotechnical Journal 40(2):403–418
38. Wood D (2004) Experimental inspiration for kinematic hardening soil models. Journal of engineering mechanics 130:656–664
39. Yao YP, Hou W, Zhou AN (2009) Uh model: three-dimensional unified hardening model for overconsolidated clays. Géotechnique 59(5):451–469
40. Yu HS (1998) CASM: A unified state parameter model for clay and sand. International journal for numerical and analytical methods in geomechanics 22(8):621–653
41. Zytynski M, Randolph M, Nova R, Wroth C (1978) On modelling the unloading-reloading behaviour of soils. International Journal for Numerical and Analytical Methods in Geomechanics 2(1):87–93